AIAA JOURNAL
Vol. 41, No. 11, November 2003

Small-Scale Airfoil Aerodynamic Efficiency Improvement by Surface Temperature and Heat Transfer

Jongmin Kim,* Zvi Rusak,† and Nikhil Koratkar‡
Rensselaer Polytechnic Institute, Troy, New York 12180-3590

The improvement of aerodynamic efficiency of small-scale airfoils using surface temperature and heat transfer is investigated using numerical simulations, asymptotic analysis, and experimental work. The basic idea is to take a direct advantage of heat transfer that dominates microscale systems to enhance lift, reduce drag, and increase the envelope of operation of airfoils. This is achieved by cooling the upper surface and heating the lower surface of the airfoil. The numerical simulations show that, although varying surface temperature does not produce significant impact at the full-scale (Reynolds numbers $> 10^6$), because the thickness of the thermal boundary layer is very small compared to the airfoil chord, its effect is very pronounced at the microscale, where the thermal and velocity boundary layers are larger. The asymptotic theory demonstrates that most of the effect actually comes from the heat transfer in the much smaller nose region of the small-scale airfoil. The experimental apparatus consists of a microrotor system that uses the Peltier effect to produce different temperatures on the surfaces of the blades. The experimental measurements show good agreement with numerical predictions.

Nomenclature

A	=	α/δ
A_k	=	coefficients of the Fourier series expansion of the thickness function, $t(x/c)$
C_d	=	sectional drag coefficient
C_l	=	sectional lift coefficient
Cp	=	pressure coefficient, $(p - p_\infty)/(\rho_\infty U_\infty^2/2)$
c	=	airfoil chord
F	=	airfoil shape function
h^2	=	$R_c/(2\delta^2 c)$
L/D	=	lift-to-drag ratio
M	=	upstream flow Mach number
R_c	=	airfoil nose radius of curvature
Re	=	Reynolds number
Re_M	=	modified Reynolds number, $Re\ R_c/c$
Pr	=	Prandtl number
T	=	temperature
t	=	airfoil thickness function
V	=	velocity
w_n	=	coefficients of the Fourier series expansion of the airfoil's camber line, $C_a(x/c)$
x	=	axial coordinate
y	=	vertical coordinate
α	=	angle of attack
α_M	=	modified angle of attack
β^2	=	$1 - M^2$
δ	=	airfoil thickness ratio
ρ	=	density

Subscripts

cp	=	property associated with common part
l	=	property associated with the lower surface
u	=	property associated with the upper surface
wl	=	property associated with the parabola lower surface
wu	=	property associated with the parabola upper surface

Superscript

$*$	=	property associated with the inner solution near the airfoil's nose

Received 30 December 2002; revision received 22 May 2003; accepted for publication 2 June 2003.

*Graduate Research Assistant, Department of Mechanical, Aerospace, and Nuclear Engineering; kimj7@rpi.edu. Student Member AIAA.

†Professor, Department of Mechanical, Aerospace, and Nuclear Engineering; rusakz@rpi.edu. Associate Fellow AIAA.

‡Assistant Professor, Department of Mechanical, Aerospace, and Nuclear Engineering; koratn@rpi.edu. Member AIAA.

Introduction

ONE of the key aspects of defense planning in the 21st century is the use of swarms of unmanned aerial vehicles that operate in concert with military forces in the battlefield. These unmanned flight vehicles are indispensable for aerial reconnaissance, covert imaging, battlefield management, and damage assessment. Small-scale vehicles can also be used by civil agencies as information and communication systems, traffic control systems, and biochemical sensors in the field or where regular vehicles do not have the necessary access.

Recent advances in system miniaturization along with emerging microdigital electronics technology has also generated interest in development of very small-scale micro-air-vehicles (MAVs) with maximum wing-span or rotor diameter less than 6 in. (15.24 cm). Two types of MAV configurations have been explored in the literature: fixed-wing configurations such as the Black Widow[1] and rotary-wing designs such as the MICOR,[2] Kolibri,[3] and the ISTAR.[4] Rotary-wing configurations are particularly attractive for battlefield surveillance and urban intelligence gathering because of their ability to hover and loiter.

The relatively low-Reynolds-number viscous flow[5–7] encountered by flight vehicles at the microscale render them inefficient and incapable of sustained and controllable flight. This work is aimed at demonstrating substantial improvements in aerodynamic efficiency of micro-flight-vehicles. We propose a novel concept featuring the control of airfoil surface temperature and heat transfer to improve performance. The basic idea is to take a direct advantage of heat transfer that dominates microscale systems to enhance lift, reduce drag, and increase the envelope of operation of airfoils. This paper describes a coupled computational and theoretical approach to explore the mechanism by which surface temperatures and heat transfer improves the aerodynamic performance of small-scale airfoils.

Previous work[8] has shown that the aerodynamic efficiency of microscale rotors is an order of magnitude lower than their full-scale counterparts. Spin testing of 6-in. (15.24-cm)-diam microrotors with both baseline NACA 0012 as well as advanced geometry Eppler-61

airfoil sections was conducted. The maximum L/D ratio that was generated for the rotor with Eppler-61 airfoil was only about 10 ($C_l \sim 0.96$ and $C_d \sim 0.1$ at $Re = 3.3 \times 10^4$), and the performance of the baseline NACA 0012 airfoil was even 50% lower at the same test conditions. These results are also consistent with recent test data presented by Young et al.[9] These performance indices are much lower than full-scale high-performance airfoils that exhibit L/D ratios in the range of 50–150. The reason for this being that in flows below Reynolds numbers of 5×10^4 the viscous effects become dominant, leading to severe drag penalties, flow separation at very low sectional angles of attack, and a smaller envelop of operation.

Given the poor aerodynamic efficiency ($L/D < 10$), low figure of merit (ratio of induced to total power[10] <0.5) of microscale rotors and limitations of current battery technology,[11,12] it is not possible to meet the flight envelope[8] for MAVs due to extreme power requirements. With present efficiency levels the maximum endurance demonstrated by battery powered MAVs has been 22 min (Ref. 1) [only 35% of the Defense Advanced Research Projects Agency (DARPA) goal of 60 min autonomous flight]. Therefore, it is critical to develop technologies to improve MAV aerodynamic efficiency to enable efficient, sustained, and controllable flight at the microscale. This project proposes a novel concept featuring control of airfoil surface temperature and heat transfer to achieve substantial improvements in MAV aerodynamic efficiency.

For microscale aerodynamic lifting surfaces, the thermal boundary-layer thickness is substantial compared to the airfoil chord and is capable of influencing the potential flow region beyond the viscous boundary layer. Therefore, by cooling the upper surface and heating the lower surface of an airfoil section (using, for example, a thermoelectric device), one could generate lower pressure on the upper surface and higher pressure on the lower surface of the airfoil section, specifically around the nose of the airfoil. This may lead to enhanced suction around the airfoil nose, generation of additional circulation and lift, and reduction in the pressure drag. Low temperature and pressure on the upper surface also means accelerated flow over the airfoil upper surface, leading to alleviation of flow separation and delay of stall to higher angles of attack.

This paper presents an extensive feasibility study that includes computational, theoretical, and experimental investigations and explores the mechanisms by which surface temperature and heat transfer improve the aerodynamic performance of small-scale airfoils. This close coupling between theory and numerical calculations helps to model the physical phenomena better and to develop a prediction tool that will guide future experiments to explore the conditions for optimal performance.

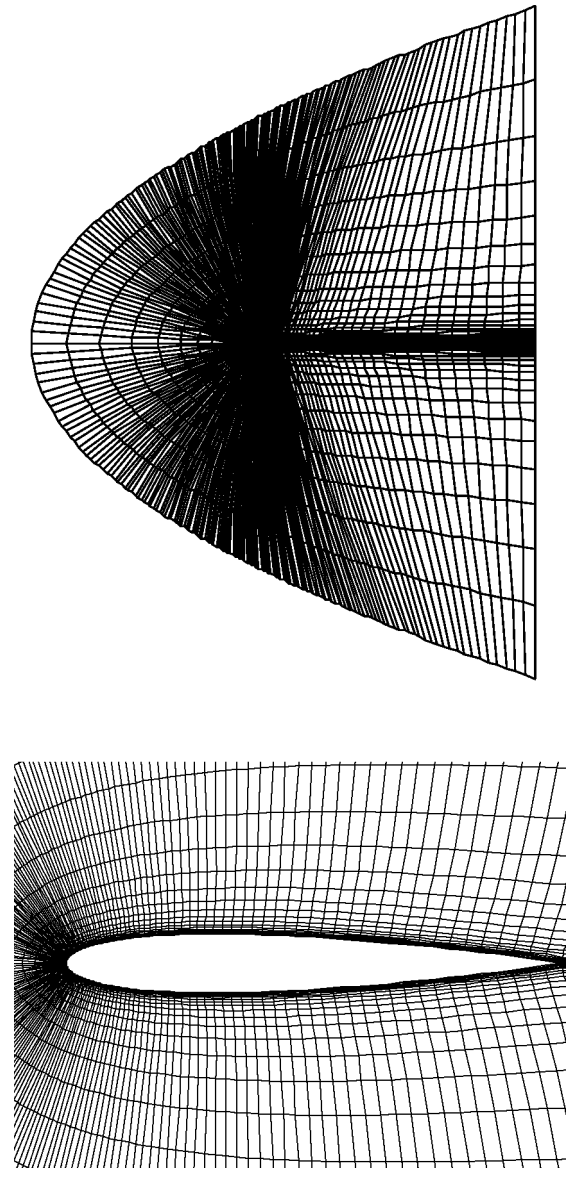

Fig. 1 Control volume and computational mesh around the airfoil.

Numerical Simulations

Numerical Model

Numerical flow simulations using the commercial Navier–Stokes flow solver FLUENT are presented. The airfoil upper and lower surfaces are described by polynomial interpolation functions to the given airfoil geometry. The far-field (outer) control surface is described by a parabolic surface of about 20 airfoil chords away from the airfoil leading edge that is cut by a vertical segment far downstream of the airfoil (Fig. 1). A structured computational grid composed of quadrilateral cells is constructed in the flow control volume between the airfoil and far-field surfaces with K radial grid lines and L circumferential grid lines (a mesh of $K \times L$). The cells are clustered near the airfoil such that the cells nearest to the surface have high aspect ratios to capture accurately the flow in the very thin thermal and velocity boundary layers. Perfect gas law is used for the equation of state, specific heat is held constant, and the Sutherland law is used to take into account effect of temperature on viscosity and thermal conductivity. In this study, temperature gradients are relatively small such that the model is accurate with the assumption of a constant specific heat. The far-field conditions model a freestream uniform flow with given freestream Mach number, static pressure, and temperature. The no penetration and no-slip boundary conditions together with a specified temperature distribution are imposed along the airfoil surfaces. An implicit and iterative, second-order procedure is used to integrate the continuity, momentum, and energy equations and calculate the steady-state fields of velocity, temperature, density, and pressure. Although the flow is predominantly laminar in the flow regime of interest, laminar flow calculations did not result in well-behaved solutions. By the use of a turbulent flow (Spalart–Allmaras) model, stable, well-converged solutions were obtained for the computations.

Numerical Verification

The code was first used to investigate a variety of baseline airfoils with no surface heating or cooling at low-Reynolds-number flows. Predictions of C_l and C_d for these cases show good match with data in the literature.[5–7] For further numerical verification, simulations were conducted with varying levels of mesh refinement. For this study, the gradients normal to the airfoil surface are much greater than those tangential to the airfoil, except near the leading and trailing edges. Consequently, the quadrilateral cells nearest the surface have very high aspect ratios. To reduce computational time and stabilize the numerical calculations, we performed initial iterations with a small Courant–Friedrichs–Lewy number (CFL) = 2, and then, after 200 iterations, the CFL was increased to 20 to speed up the convergence.

Mesh convergence studies were performed for the case of a uniform flow of air with Mach number 0.0725, pressure 1 atm, and temperature 300 K around a NACA 0012 airfoil where the upper

surface temperature is 260 K and the lower surface temperature is 340 K ($|\Delta T| = 40$ K). The flow Reynolds number is 3.3×10^4. Results of the computations with various meshes are shown in Figs. 2 and 3. Figure 2a shows the lift coefficient as a function of angle of attack. The results with a mesh of 80×40 (7200 cells) show an underprediction of the lift coefficient. However, for finer mesh of 100×50 (9800 cells) and beyond, no significant change in the solution is observed at all angles of attack (Fig. 2b). Figure 3 shows the solutions of the pressure coefficient along the airfoil surfaces for a case with 8-deg angle of attack using different meshes. The results with 7200 cells show an underprediction of the suction peak near the nose region leading to a corresponding under prediction of lift coefficient. However, for refined meshes of 100×50 and beyond, the pressure distributions are nearly identical. We conclude from Figs. 2 and 3 that a mesh of 100×50 is sufficient for a converged (mesh-independent) flow solution. This mesh is used in all of the following flow simulations.

Results of Numerical Simulations

To demonstrate the impact of surface temperature, two cases of a uniform flow of dry air with upstream Mach number 0.0725, pressure 1 atm, and temperature 300 K around a NACA 0012 section

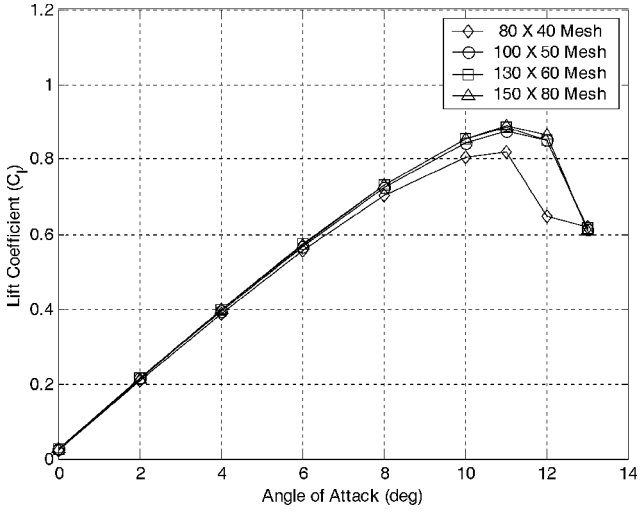

a) Computed lift coefficient vs angle of attack for various meshes

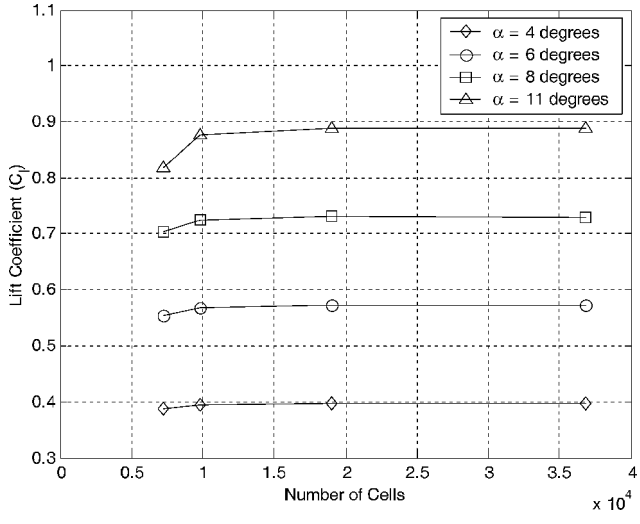

b) Convergence of lift coefficient at several different angles of attack with mesh refinement

Fig. 2 Numerical verification; lift coefficient of a NACA 0012 airfoil section with upper surface temperature of 260 K and lower surface temperature of 340 K at freestream with Mach number 0.0725, temperature 300 K, pressure 1 atm, Reynolds number 3.3×10^4, and various angles of attack.

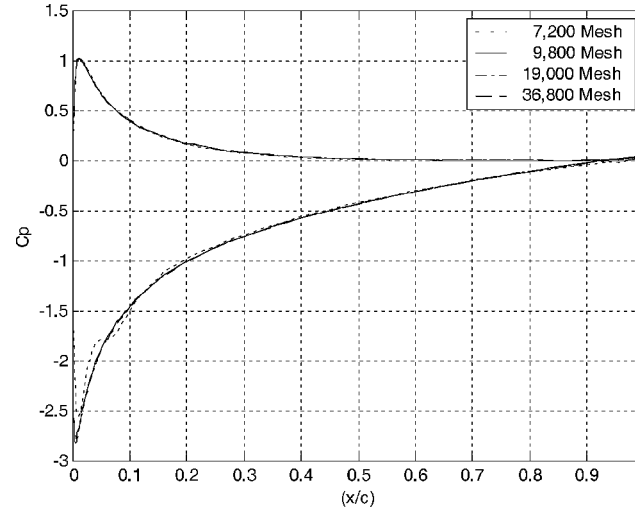

Fig. 3 Numerical verification; pressure coefficient vs nondimensional chordwise position for NACA 0012 section with upper surface temperature of 260 K and lower surface temperature of 340 K at a freestream with Mach number 0.0725, temperature 300 K, pressure 1 atm, and Reynolds number 3.3×10^4, at 8-deg angle of attack.

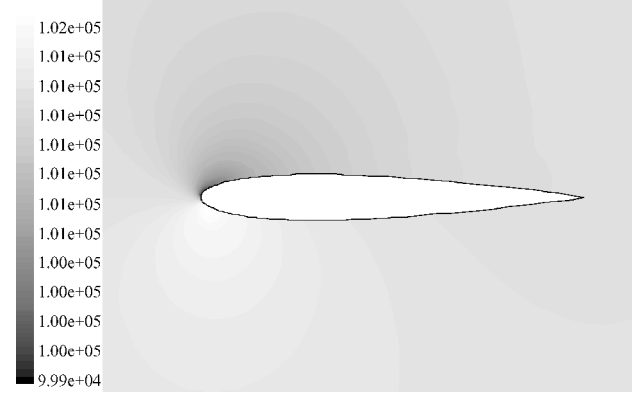

a) Surface temperature 260 K

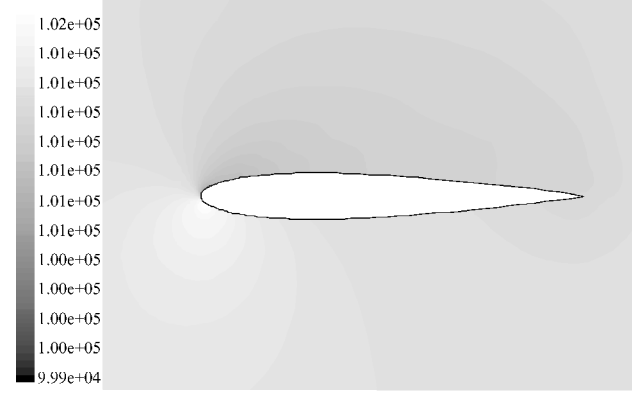

b) Surface temperature 400 K

Fig. 4 Pressure contours around a NACA 0012 airfoil in freestream with Mach number 0.0725, temperature 300 K, pressure 1 atm, Reynolds number 3.3×10^4, at 12-deg angle of attack.

at 12-deg angle of attack are considered, 1) where the surface temperature on both upper and lower surfaces is cooled to 260 K and 2) where the temperature on both surfaces is heated to 400 K. The Reynolds number in both cases is 3.3×10^4 (corresponding to an airfoil chord of 2 cm). Note that the stagnation temperature on the airfoil surfaces at the regular (no cooling or no heating) case is 300.3 K. Figures 4a and 4b show a comparison of the static pressure contours for the heated and cooled NACA 0012 airfoils. Clearly,

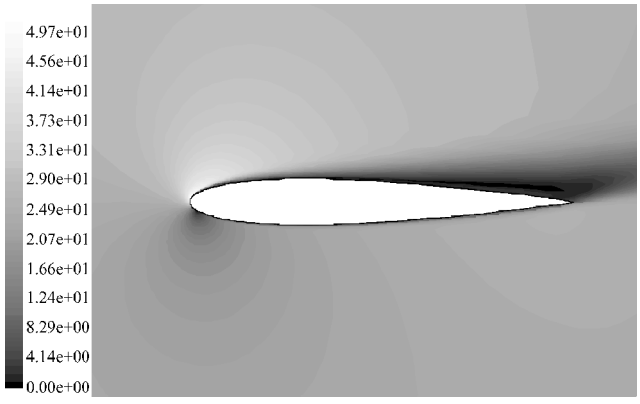

a) Surface temperature 260 K

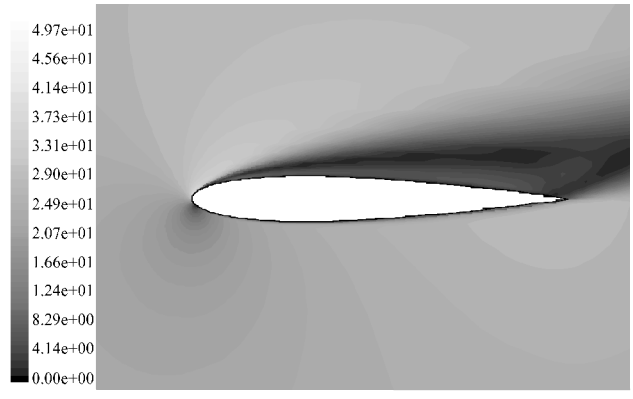

b) Surface temperature 400 K

Fig. 5 Velocity contours around a NACA 0012 airfoil in freestream with Mach number 0.0725, temperature 300 K, pressure 1 atm, Reynolds number 3.3×10^4, at 12-deg angle of attack.

the suction region on the upper surface (indicated by the localized region of dark contour lines on the upper surface of the airfoil that appears in Fig. 4a and does not appear in Fig. 4b) has expanded significantly for the cooled airfoil compared to the heated airfoil, resulting in enhanced lift. Figure 5a and 5b show the corresponding velocity profiles. The heated airfoil is in predominantly stalled flow (as is also the base case airfoil) with extensive flow separation close to the leading edge. The cooled airfoil, however, clearly shows significantly reduced separation, leading to increased lift and reduction in airfoil drag penalty. These results show that surface temperature (particularly on the upper surface of the airfoil) can have an important effect on the aerodynamic efficiency of small-scale airfoils operating at very low Reynolds numbers.

Additional computational results of flows around a NACA 0012 with full-scale (where the flow Reynolds number is 1.7×10^6 and $c = 1$ m) and a microscale airfoil (where the flow Reynolds number is 3.3×10^4 and $c = 2$ cm) are shown in Figs. 6–8 for cases where 1) the surface temperature is 300 K (the base reference case) and 2) the temperature of upper surface is at 200 K and lower surface is maintained at 400 K (a differential of 200 K). In all cases the upstream uniform flow is at Mach number 0.0725, pressure 1 atm, and temperature 300 K. Figure 6 shows the lift coefficient as a function of angle of attack for a representative full-scale and microscale airfoil. If surface temperature difference of 200 K is maintained for microscale airfoil, an improvement in lift coefficient is predicted. (Note that the absolute value of the lift increase is almost the same up to 10-deg angle of attack.) At 12-deg angle of attack, a much larger increase in lift coefficient (from about 0.66 to about 0.96) is predicted for the microscale airfoil. This is because of alleviation of flow separation and delay of stall to higher angle of attack (from about 11 to about 12 deg) by cooling the upper surface and the resulting heat transfer effect. However, no significant improvement in lift response is computed for the full-scale airfoil. Figure 7 is a comparison of results of the drag coefficient variation for the base

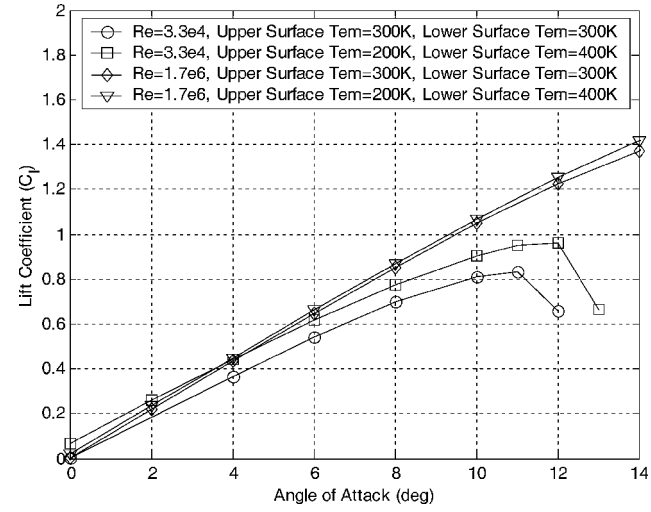

Fig. 6 Lift coefficient as function of angle of attack of NACA 0012 airfoil in freestream with Mach number 0.0725, temperature 300 K, pressure 1 atm at various Reynolds numbers and surface temperatures.

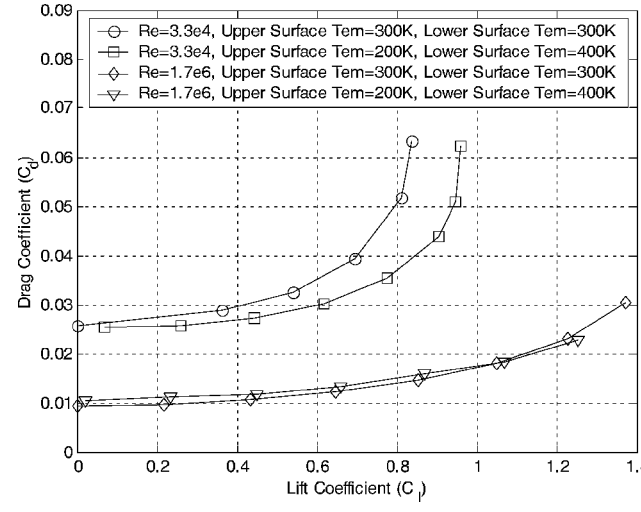

Fig. 7 Drag coefficient as function of lift coefficient of NACA 0012 airfoil in freestream with Mach number 0.0725, temperature 300 K, pressure 1 atm at various Reynolds numbers and surface temperatures.

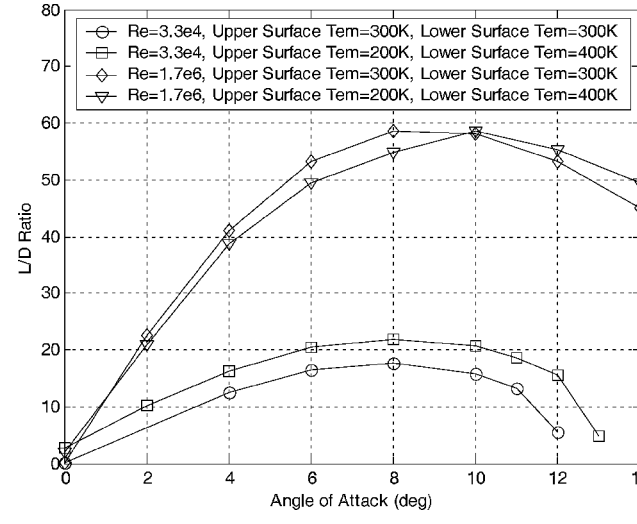

Fig. 8 Lift-to-drag ratio as function of angle of attack of NACA 0012 airfoil in freestream with Mach number 0.0725, temperature 300 K, pressure 1 atm at various Reynolds numbers and surface temperatures.

case and with surface temperature difference of 200 K. Significant decrease of drag coefficient is observed only for the microscale airfoil. Note that the drag reduction becomes more significant with increase in lift coefficient as the sectional stall angle is approached. A similar trend is described in Fig. 8 for the sectional L/D ratio. An improvement in L/D from 5.4 at the base case to 15.5 is predicted at 12-deg sectional angle of attack for the microscale airfoil.

We attribute the computed improvements of aerodynamic performance demonstrated earlier to the heat transfer at microscale, specifically near the airfoil nose, which enables the inviscid flow region beyond the velocity boundary layer to be influenced by the surface temperature and, thereby, affect the pressure distribution along the airfoil. This is shown in Fig. 9, which shows the thermal and velocity boundary layers on both the upper (200 K) and lower (400 K) surfaces of the microscale airfoil at 10% chordwise station. The baseline case (where both surfaces are at 300 K) is also shown for comparison. On the upper surface of the airfoil that is cooled to 200 K (Fig. 9a), the flow is accelerated with respect to the baseline due to exchange of thermal and kinetic energy in the flow region outside of the velocity boundary layer. In this region, the flow has significantly higher axial speed compared to the baseline. This means that the pressure at the edge of the velocity boundary layer (which is also the airfoil surface pressure at this point) is lower on the upper cooler surface than in the baseline case. The converse is true on the lower surface that is heated to 400 K (as shown in Fig. 9b). This differential pressure is responsible for the generation of additional lift (Fig. 6). The acceleration of the flow on the upper surface also results in delay of flow separation to higher angles of attack (Figs. 6–8).

Note that the improvement in performance is realized only at the microscale. Figure 10 shows the thermal and velocity boundary layers for the full-scale airfoil (Reynolds number 1.7×10^6) at 10% chordwise station. The upper and lower surface temperatures are the same as in the microscale airfoil; however, both the thermal and velocity boundary layers are much thinner (relative to the airfoil chord) in the higher-Reynolds-number flow as compared to the microscale. Because of this, the acceleration (Fig. 10a) of the flow on the upper cooler surface (200 K) and deceleration (Fig. 10b) on the lower warmer surface (400 K) due to heat transfer effects are quite weak, and as a result, the surface pressure changes from the base case with no difference in surface temperature are very small. This shows that, at the larger scales, heat transfer near the airfoil nose has a much more limited influence on the velocity and pressure distributions downstream of the nose region than in the case of a small-scale airfoil. The objective of our study is to take a direct advantage of the small scales (associated with micro-flight-vehicles) in conducting heat to increase the lift, reduce the drag, and increase the L/D ratios.

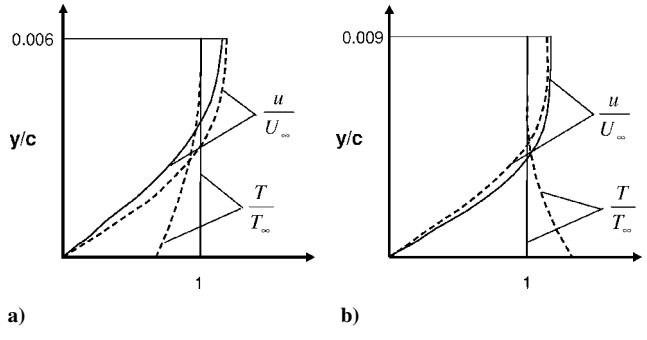

Fig. 9 Thermal and velocity boundary layers at 10% chordwise station of NACA 0012 section in freestream with Mach number 0.0725, temperature 300 K, pressure 1 atm, and Reynolds number 3.3×10^4, at 0-deg angle of attack: a) upper surface of microscale airfoil; ——, baseline case (300 K) and – – –, thermally activated (200 K) case; and b) lower surface of microscale airfoil; ——, baseline case (300 K) and – – –, thermally activated (400 K) case.

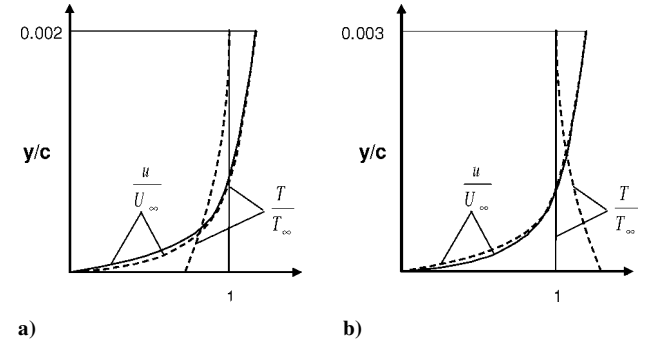

Fig. 10 Thermal and viscous boundary layers at 10% chordwise station of NACA 0012 section in freestream with Mach number 0.0725, temperature 300 K, pressure 1 atm, and Reynolds number 1.7×10^6, at 0-deg angle of attack: a) upper surface of full-scale airfoil; ——, baseline case (300 K) and – – –, thermally activated (200 K) case; and b) lower surface of full-scale airfoil; ——, baseline case (300 K) and – – –, thermally activated (400 K) case.

Theoretical Study

To investigate the mechanism by which surface temperature and heat transfer affect the airfoil's performance, we developed a multiscale matched asymptotic analysis for a moderate-Reynolds-number ($Re \gg 1$) compressible flow of a thermally perfect gas (dry air) around a small-scale thin airfoil at low and moderate angles of attack (before stall occurs). The airfoil geometry is given by $y = \delta c F_{u,l}(x/c)$ for $0 \le x \le c$, where the upper and lower surface shape functions $F_{u,l}(x/c)$ are described by $F_{u,l}(x/c) = C_a(x/c) - Ax/c \pm t(x/c)$ with $0 < \delta \ll 1$ and $A = \alpha/\delta$. Here, $C_a(x/c)$ is the camber-line function, $t(x/c)$ is the thickness function, and the airfoil nose is parabolic. The airfoil is given in a uniform stream of air with Mach number M, temperature T_∞, and pressure p_∞. The freestream flow speed is $U_\infty = M\sqrt{(\gamma R T_\infty)}$, where γ is ratio of specific heats and R is the specific gas constant for air; density is $\rho_\infty = p_\infty/(RT_\infty)$; viscosity is $\mu_\infty = \mu(T_\infty)$; specific heat is $C_{p\infty}$; and heat conduction coefficient is $\lambda_\infty = \lambda(T_\infty)$. The airfoil's upper surface temperature is set at T_{wu} and along the lower surface it is set at T_{wl}. Asymptotic expansions of the velocity components and the thermodynamic properties are constructed in an outer region around most of the airfoil and in an inner region near the nose, in terms of the airfoil small thickness ratio δ. The analysis extends the work of Rusak[13] on the subsonic flow around a thin airfoil to include the effect of the surface temperature and heat transfer on the flowfield.

In the outer expansion, we use the reference parameters c, U_∞, T_∞, p_∞, ρ_∞, μ_∞, and λ_∞ to scale the axial and vertical distances, velocity components, temperature, pressure, density, viscosity, and heat conduction coefficent, respectively. There, the steady-state dimensionless equations governing the flow are

$$\nabla \cdot (\rho \boldsymbol{V}) = 0$$

$$\rho \boldsymbol{V} \cdot \nabla \boldsymbol{V} + (1/\gamma M^2)\nabla p = (1/Re)\nabla \cdot \left(\mu\left\{2[\nabla \boldsymbol{V} + (\nabla \boldsymbol{V})^T] - \tfrac{2}{3}\boldsymbol{I}(\nabla \cdot \boldsymbol{V})\right\}\right)$$

$$\rho \boldsymbol{V} \cdot \nabla T - [(\gamma - 1)/\gamma]\boldsymbol{V} \cdot \nabla p = (1/Re)(1/Pr)\nabla \cdot (\lambda \nabla T) + (\gamma - 1)(M^2/Re)\Phi$$

$$p = \rho T \tag{1}$$

Here $\boldsymbol{V}$ is the dimensionless velocity vector, ρ, p, T, μ, and λ are the dimensionless density, pressure, temperature, viscosity, and heat conduction coefficient, $Re = \rho_\infty U_\infty c/\mu_\infty$, $\mathrm{Pr} = \mu_\infty C_{p\infty}/\lambda_\infty$, $\boldsymbol{I}$ is the unit tensor, and Φ is the dimensionless dissipation function. Typically $Re \gg 1$, and the effects of surface temperature, viscosity, and heat conduction are localized to the very thin thermal and velocity boundary layers and play only a secondary (or even smaller) role in determining the pressure distribution along the airfoil. Except for the thin boundary layers near the airfoil surfaces and the airfoil's nose region, the flow in the outer region, around most of the airfoil,

is dominated by the inviscid version of Eqs. (1):

$$\nabla\cdot(\rho\boldsymbol{V})=0,\qquad \rho\boldsymbol{V}\cdot\nabla\boldsymbol{V}+(1/\gamma M^2)\nabla p=0$$
$$\rho\boldsymbol{V}\cdot\nabla T-[(\gamma-1)/\gamma]\boldsymbol{V}\cdot\nabla p=0,\qquad p=\rho T \tag{2}$$

Actually, because the upstream flow is uniform, the flow is also irrotational and potential. The solution of Eq. (2) with the no penetration condition along the airfoil surfaces and the upstream uniform flow conditions at the far field provides the far-field conditions for the boundary layers. Specifically, the pressure distribution along the airfoil surfaces from this inviscid solution is also the pressure distribution at the edge of the boundary layers.

Moreover, because typically the airfoil's thickness ratio is small ($0<\delta\ll 1$), it can be shown (see Rusak[13]) that the solution of Eq. (2) in the outer region (around most of the airfoil except for the nose region) is dominated by the classical subsonic linear airfoil theory. Then, the pressure coefficient along most of the airfoil's upper (u) and lower (l) surfaces (in the range $\delta<x/c<1$) may be approximated in the leading-order terms by

$$Cp_{u,l}\left(\frac{x}{c}\right)=-2\frac{\delta}{\beta}\left\{h(1+2\cos\theta)+2\sum_{k=2}^{\infty}A_{2k-1}\times\left[\frac{\sin(2k-1)\theta-\sin\theta}{\sin\theta}\right]+2\sum_{k=2}^{\infty}A_{2k}\left[\frac{\sin(2k\theta)-\sin(2\theta)}{\sin\theta}\right]+(-1)^m A\left[w_0\frac{1+\cos\theta}{\sin\theta}-\sum_{n=1}^{\infty}(-1)^n w_n\sin(n\theta)\right]\right\} \tag{3}$$

where

$$\frac{x}{c}=\frac{1-\cos\theta}{2},\qquad 0<\theta<\pi$$
$$A_n=\frac{2n}{\pi}\int_0^{\pi}t\left(\frac{x}{c}\right)\sin n\theta\,\mathrm{d}\theta,\qquad w_0=1-\frac{1}{\pi A}\int_0^{\pi}Ca'\left(\frac{\xi}{c}\right)\mathrm{d}\theta$$
$$w_n=\frac{2n}{\pi A}\int_0^{\pi}Ca'\left(\frac{\xi}{c}\right)\cos n\theta\,\mathrm{d}\theta$$

Also, $m=1$ for the upper surface and $m=-1$ for the lower surface. Note that the linear theory solution (3) exhibits a singular behavior as x/c approaches the leading edge, that is, $Cp_{u,l}(x/c)\sim(-1)^m(2\alpha\, w_0\sqrt{(c/x)}/\beta)$ as x/c approaches zero.

In the inner region around the airfoil's nose ($0\le x/c<R_c/c$), scaled coordinates and flow parameters are used to describe correctly the local nonlinear behavior of the flow and the dominant effect of heat transfer around the nose. There, we use the nose radius of curvature $R_c=2\delta^2h^2c$ to scale the axial and vertical coordinates, $x^*=x/R_c$ and $y^*=y/R_c$. In terms of these dimensionless coordinates, and the scaling parameters U_∞, T_∞, p_∞, ρ_∞, μ_∞, and λ_∞ for the velocity components, temperature, pressure, density, viscosity, and heat conduction coefficient, respectively, the problem in the nose region becomes in the leading order the flow of a compressible, viscous, and heat conducting stream described by the dimensionless equations

$$\nabla^*\cdot(\rho^*\boldsymbol{V}^*)=0$$
$$\rho^*\boldsymbol{V}^*\cdot\nabla^*\boldsymbol{V}^*+(1/\gamma M^2)\nabla^*p^*=(1/Re_M)\nabla^*\cdot\left(\mu\left\{2[\nabla^*\boldsymbol{V}^*+(\nabla^*\boldsymbol{V}^*)^T]-\tfrac{2}{3}I(\nabla^*\cdot\boldsymbol{V}^*)\right\}\right)$$
$$\rho^*\boldsymbol{V}^*\cdot\nabla^*T^*-[(\gamma-1)/\gamma]\boldsymbol{V}^*\cdot\nabla^*p^*=(1/Re_M)(1/Pr)\nabla^*\cdot(\lambda\nabla^*T^*)+(\gamma-1)\left(M^2/Re_M\right)\Phi^*$$
$$p^*=\rho^*T^* \tag{4}$$

Equations (4) show that the inner flow problem is characterized by the same Prandtl number Pr but with a modified Reynolds number $Re_M=ReR_c/c$, which is much smaller than Reynolds number Re. In this way, the local viscous and heat transfer effects around the airfoil nose are correctly accounted for. Moreover, in the inner region, to the leading orders, the airfoil is described by a canonic parabola $y^*=\sqrt{(2x^*)}$. Along the parabola upper surface the temperature is T_{wu} and along the lower surface it is T_{wl}, and the no-penetration and no-slip conditions are satisfied. Also, in the inner region, the upstream flow is uniform with Mach number M (of the flow around the airfoil), modified angle of attack α_M, temperature T_∞, and pressure p_∞. The inner flow equations (4) are solved numerically using the commercial code FLUENT. The solution results in the distribution of the pressure coefficient $Cp^*(x^*;\, M,\, \alpha_M,\, Re_M,\, Pr,\, T_{wu}/T_\infty,\, T_{wl}/T_\infty)$ along the parabola surfaces that is strongly affected by modified Reynolds number, Re_M and the surface temperatures. Also note that for most relevant applications modified Reynolds number is sufficiently large ($Re_M>100$) such that thin velocity and thermal boundary layers form along the parabola surfaces as x^* increases above 10 and the flow around the parabola and outside these boundary layers is approximately inviscid and potential. Therefore, following Rusak,[13] the pressure coefficient $Cp^*(x^*;\, M,\, \alpha_M, Re_M, Pr, T_{wu}/T_\infty, T_{wl}/T_\infty)$ along the parabola surfaces decays as $(-1)^m[Aw_0\sqrt{(2/x^*)}/\beta h]$ as x^* increases.

A matching between the inner and outer asymptotic expansions for the pressure distribution in an overlap region between the two regions ($R_c<x/c<\delta$) is established. It is found that the two expansions have a common part of the pressure distribution along the airfoil surface, which is approximated by

$$Cp_{\mathrm{cp}}(x/c;\, M,\, \delta,\, A)=(-1)^m\left(2\alpha\, w_0\sqrt{c/x}\big/\beta\right) \tag{5}$$

where $m=1$ for the upper surface and $m=-1$ for the lower surface. Note that the common part given by Eq. (5) coincides with the singular behavior of $Cp_{u,l}$ as x approaches zero and with the decay of Cp^* as x^* increases. The asymptotic matching results also in a uniformly valid asymptotic composite solution of the pressure distribution along the entire airfoil chord that can be approximated by

$$Cp(x/c;\, M,\, \alpha,\, \delta,\, Re,\, Pr,\, T_{wn}/T_\infty,\, T_{wl}/T_\infty)=Cp^*\left(x^*;\, M,\, \alpha_M,\, Re_M,\, Pr,\, T_{wn}/T_\infty,\, T_{wl}/T_\infty\right)+[Cp_{u,l}(x/c)-Cp_{\mathrm{cp}}(x/c;\, M,\, \delta,\, A)]\,V^*(x^*)\rho^*(x^*) \tag{6}$$

Here,

$$V^*=\sqrt{1-\left[2\big/(\gamma-1)M_\infty^2\right]\left\{\left[1+\left(\gamma M_\infty^2\big/2\right)-Cp^*\right]^{(\gamma-1)/\gamma}-1\right\}}$$
$$\rho^*=\left[1+\left(\gamma Ma_\infty^2\big/2\right)Cp^*\right]^{(1/\gamma)} \tag{7}$$

They represent the nondimensional velocity and density at the edge of the thin boundary layers that form in the inner region along the parabola surfaces and are functions of Cp^* only. Equations (7) are derived from the potential (isentropic) flow relationships between pressure, density, and velocity. Formula (6) shows that the pressure distribution along the airfoil is composed of a nonlinear combination of the linear theory solution and the nose solution. As the leading edge of the airfoil is approached (x tends to zero and $0<x/c<R_c/c$) the common part pressure Cp_{cp} cancels the nose singularity of the outer linear pressure coefficient solution both on the upper and lower surfaces of the airfoil. Also, in this region, V^* is small and tends to zero near the stagnation point. Therefore, the dominant term in the leading-edge region is the parabola pressure coefficient Cp^*, which is strongly affected by the surface temperature distribution around the nose and the modified Reynolds number. As x is increased beyond the leading-edge region, $\delta<x/c<1$, the parabola density ρ^* and velocity V^* tend to one, and the common part pressure Cp_{cp} cancels the parabola pressure Cp^*. Therefore, the dominant term in the outer region is the classical subsonic linear theory solution $Cp_{u,l}$. In the intermediate region, $R_c/c<x/c<\delta$, the pressure changes uniformly from Cp^* to $Cp_{u,l}$.

The present theory explains the mechanism by which surface temperature changes improve the aerodynamic performance of small-scale airfoils. The primary effect is of the surface temperature along the airfoil's nose in the range $0 < x/c < R_c$. There, the reduced modified Reynolds number and surface temperature distribution strongly affect the flow structure and the pressure distribution along the nose. For example, cooling the upper surface ($T_{wu} < T_\infty$), or warming the lower surface ($T_{wl} > T_\infty$), or enforcing both accelerates the flow over the upper surface of the nose and creates suction and decelerates the flow along the lower surface of the nose and increases the high-pressure region around the stagnation point. Thereby, the airfoil lift is increased, and drag is decreased. Note that this effect is strongly related to the small scale of the airfoil and its nose through the relatively small value of Reynolds number Re and its further decreased value Re_M in the nose region. It is clear that when the scale of the airfoil is much larger and Reynolds number Re is large ($Re > 10^6$) this effect disappears because Re_M is also very large and the heat transfer from the surface to the flow is localized even around the nose and does not significantly affect the nose pressure distribution.

The present analysis also results in a simplified but accurate prediction tool for the distribution of pressure along the airfoil [Eq. (6)] and the additional lift resulting from the surface temperatures and heat transfer. We demonstrate this point in Figs. 11–13. For the

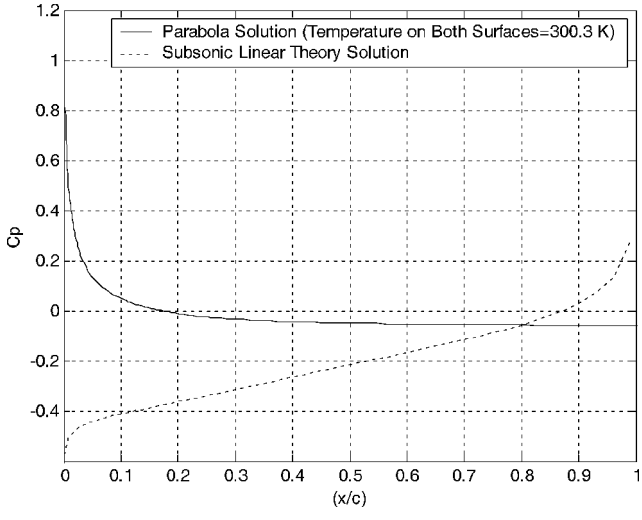

a) Parabola problem and subsonic linear theory without surface temperature difference

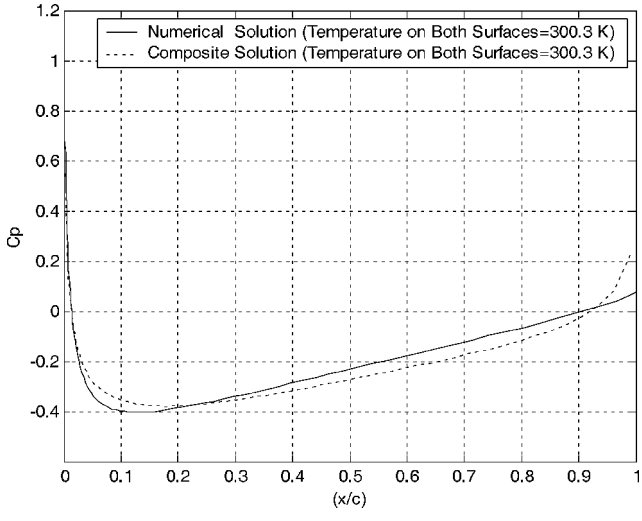

b) Numerical and composite simulation without surface temperature difference

Fig. 11 Pressure coefficient of NACA 0012 airfoil without surface temperature difference, Mach number 0.0725 and Reynolds number 3.3×10^4, at 0-deg angle of attack.

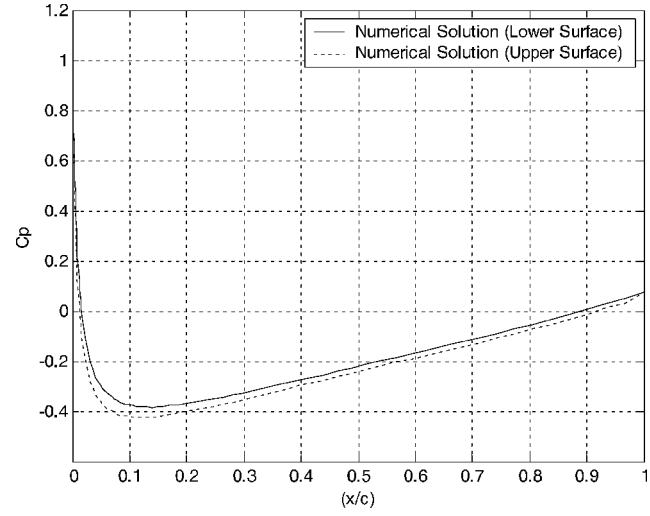

a) Numerical simulation with upper surface temperature 260 K and lower surface temperature 340 K

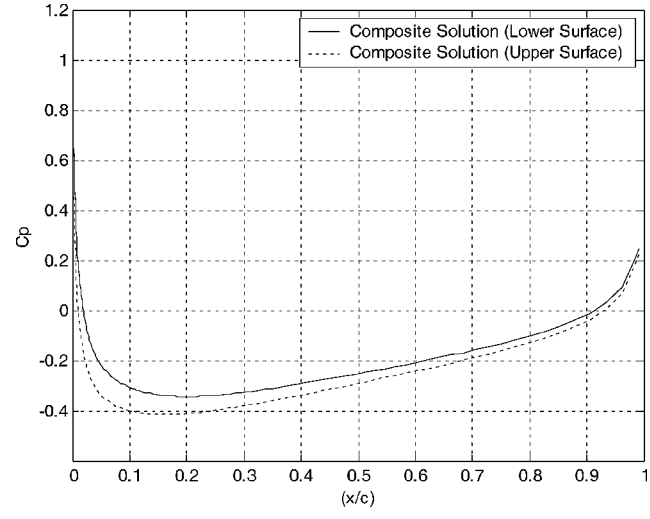

b) Composite simulation with upper surface temperature 260 K and lower surface temperature 340 K

Fig. 12 Pressure coefficient of NACA 0012 airfoil with surface temperature difference, Mach number 0.0725 and Reynolds number 3.3×10^4, at 0-deg angle of attack.

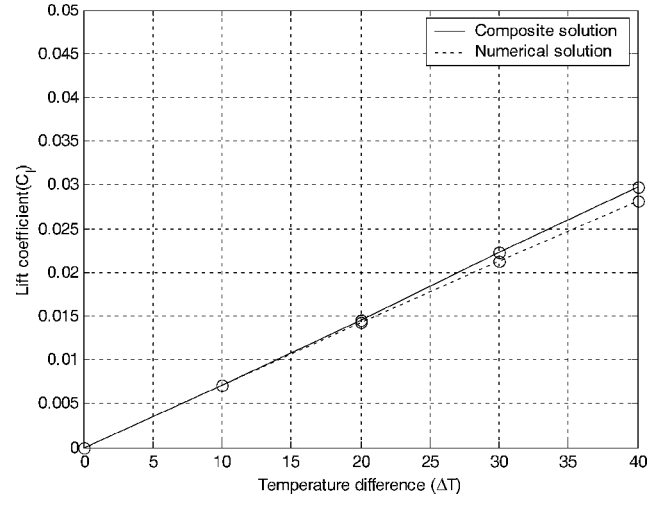

Fig. 13 Lift coefficient variation of NACA 0012 airfoil, composite and numerical simulation, Mach number 0.0725, and Reynolds number 3.3×10^4, at 0-deg angle of attack.

baseline conditions the Mach number is 0.0725, Reynolds number is 3.3×10^4, chord is 2 cm, temperature on both surfaces is 300.3 K (as the far-field temperature), and the airfoil is a NACA 0012 at 0 angle of attack. Figure 11a shows results for subsonic linear theory as well as results of the canonic parabola solution. Figure 11b shows a comparison of the pressure distribution from the numerical solution and the composite solution (based on the multiscale matched asymptotic analysis using parabola and linear theory solutions). Good correlation is achieved between the theory and numerical solution for the baseline condition. Note that, because the angle of attack is 0 deg and no temperature differential is imposed for the baseline case, the pressure distributions for the upper and lower surfaces are identical, that is, no generation of lift for baseline condition.

Next, a temperature differential is imposed such that upper surface temperature T_{wu} is 260 K and lower surface temperature T_{wl} is 340 K. Results from the numerical simulation and composite solution are shown in Figs. 12a and 12b, respectively. Both the numerical and composite solutions show that the upper surface pressure has reduced and the lower surface pressure has increased compared to the baseline condition (Fig. 11b). It is this differential pressure that is responsible for the generation of lift. Both the numerical and composite solutions indicate that the majority of the lift comes from the nose region (0–20% chord) indicated by the large pressure differential between the upper and lower airfoil surfaces in this region. Outside of the nose region, the surface temperature effects are small and the pressure is dominated by the linear-theory solution.

We have also investigated the relationship between the lift increment and the differential between the airfoil surface temperature and upstream flow temperature. Figure 13 shows the increase in airfoil lift coefficient due to prescribed temperature differential using both numerical and composite solutions at an angle of attack of 0 deg. The boundary conditions are imposed such that the upper airfoil surface temperature is decreased by ΔT, while the lower surface temperature is increased by ΔT. Both numerical simulations and asymptotic composite model show good agreement. The lift increment increases linearly with temperature difference. Simulations were also conducted at higher angles of attack, and it was determined that, in the attached flow regime (before the onset of stall), the lift increment increases linearly with the temperature differential.

Our studies using the asymptotic approach show the relevance and accuracy of the theory. The prediction tool developed will be used in the future to identify optimal surface temperature changes for a maximal increase in lift and L/D ratio, as well a delay of stall to higher angles of attack. These optimal conditions will be applied in the experiments to verify the theoretical predictions as well as demonstrate that the predicted improvements can be achieved in the design of small-scale airfoils and rotors.

Experimental Validation

To generate test data to validate the computational and theoretical results, microrotor blades with 6-in. (15.24-cm) diameter are spin tested. The microrotor blades are fabricated using a commercially available thermoelectric alloy material that exhibits the Peltier effect (see Ref. 14) under electrical activation. The Peltier effect occurs when any two members of the thermoelectric series are connected to form a junction. In the presence of a current, a temperature difference between the junctions is produced. This effect can be used to cool a system by drawing heat from one side of the junction to the other through the application of a small electrical charge. In addition, reversing the polarity of the applied dc voltage reverses the direction of the heating and cooling, a feature that makes these devices ideal for controlling temperature or in processes that require both heating and cooling of a medium. The microblades are fabricated such that the thermoelectric junction associated with the Peltier effect is located at the centerline of the airfoil section. Therefore, application of a control voltage across the thickness of the airfoil results in a temperature differential between the upper and lower airfoil surfaces. This temperature differential influences the rotor aerodynamic performance, and this can be measured and compared with the computational results.

Microrotor Test Platform

The experimental setup consists of a highly sensitive load cell (least count 0.02 g) for measuring rotor thrust, a laser light source coupled to a frequency counter to measure rotor speed and a micro-coreless-dc motor with associated fixtures that connect the microblades to the motor output spindle. The motor is driven by means of a dc power supply. Figure 14 shows the microrotor test platform instrumented with a slip ring to enable electrical activation of rotor blades in the rotating frame. The diameter of the microrotor is restricted to a maximum of 6 in. (15.24 cm) to conform to the specification of DARPA's MAV program. A clearance of 10 in. (more than twice the rotor radius) is maintained to eliminate ground effect.[15] Figure 15 shows a close up view of the microrotor blades, micro-dc-motor and hub attachment fixtures. The blades can be connected to the hub at adjustable collective pitch settings.

The microrotor blades are tested at 1000 rpm in room temperature low-humidity environment. The planform is rectangular (no taper or sweep), aspect ratio is 2 [7.63-cm (3-in.) radius and 3.81-cm (1.5-in.) cord], camber is 0%, and the blades are untwisted. For this case the room temperature is 297 K, the Mach number is 0.018, and Reynolds number is 1.67×10^4. The tests are conducted for two cases: 1) upper surface temperature is 290 K and lower surface temperature is 360 K and 2) upper surface temperature is 360 K and lower surface temperature is 290 K. We have demonstrated that a 3.7-V dc activation results in a 70 K temperature differential between the upper and lower surfaces of the Peltier alloy material. This enables the required temperatures (290, 360 K) to be maintained on opposing surfaces of the microblades during the spin test.

Test Results

The microrotor blades are tested at several blade pitch settings ranging from 9 to 15 deg. For each pitch setting, the rotor thrust is measured, both with and without control of surface temperature. The measured rotor thrust is used to estimate the sectional lift at a

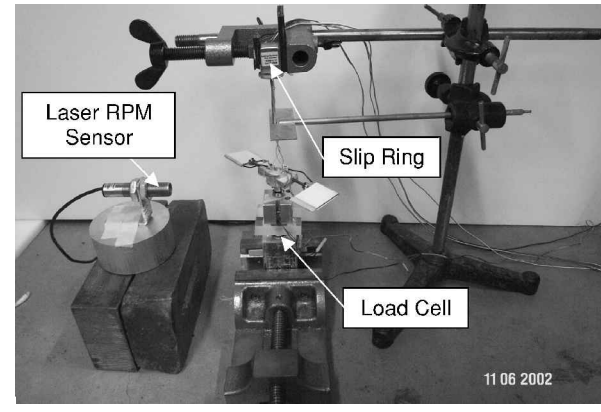

Fig. 14 Microrotor test platform (load cell, revolutions per minute sensor and slip ring).

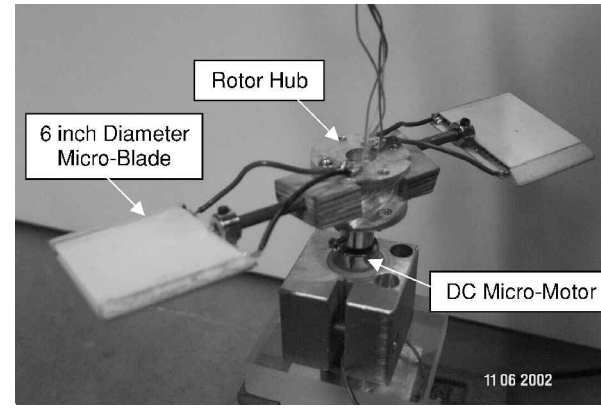

Fig. 15 Microrotor blade assembly and hub fixtures.

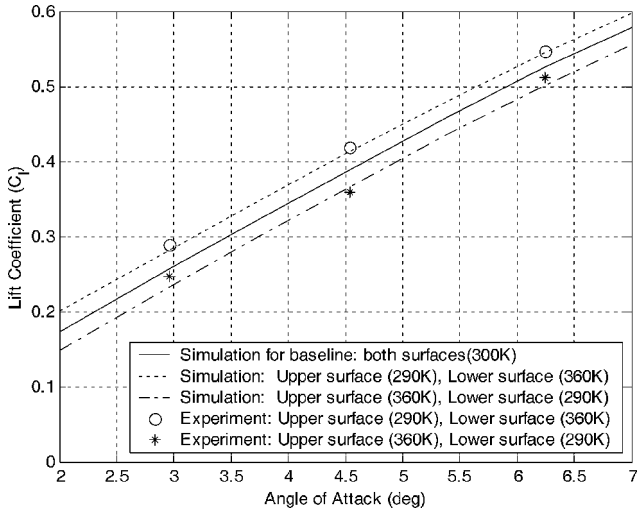

Fig. 16 Lift coefficient vs angle of attack with 70 K surface temperature difference with Mach number 0.01786 and Reynolds number 1.6×10^4.

typical section along the blade span using combined blade element momentum theory[16] in hover. Figure 16 shows the measurements on the lift coefficient at a typical section (75% radius) both with and without activation of surface temperature for several different angles of attacks. The effective angle of attack at the blade section of interest is estimated from blade element momentum theory by subtracting the inflow angle (created by the rotor downwash) from the blade pitch setting. The angle-of-attack range for the present testing is between 2 and 7 deg, which is below the onset of airfoil stall. Blade surface temperature was imposed by the application of a 3.7-V dc input to the Peltier module. Depending on the polarity of the voltage connection, two types of tests are conducted: 1) Upper surface of the blades is cooled and the lower surface is heated. (For this case we expect increase in airfoil lift.) 2) Upper surface is heated and lower surface is cooled. (For this case we expect decrease in lift.) The test results shown in Fig. 16 confirm that this is indeed the case. The predictions of the numerical simulations also show good correlation with the measurements. For example, at an effective angle of attack of 4.5 deg (corresponding to blade pitch setting of 12 deg), the estimated increase of lift coefficient is 6.0%, with an upper surface temperature of 290 K and lower surface temperature of 360 K, and −5.8%, with an upper surface temperature of 360 K and lower surface temperature of 290 K. The experimental results show 7.7 and −7.7% for each case. The variation of the lift results from the baseline condition (297.3 K surface temperature) for the two test cases is quite symmetrical as predicted by the simulations. Also the absolute value of the lift increase/decrease, ΔC_l, is fairly constant, depends mainly on the temperature differential, and is not very sensitive to angle of attack (in the attached flow regime) as predicted by the numerical simulations and the asymptotic analysis developed in this paper.

Conclusions

The present simulations and theoretical predictions indicate that although varying surface temperature does not produce significant impact at full-scale (Reynolds numbers $> 10^6$), because the thickness of the thermal and velocity boundary layers is very small compared to the airfoil chord, its effect is very pronounced at microscale. The asymptotic theory shows that most of the effect actually comes from the heat transfer in the much smaller nose region of the small-scale airfoil. We demonstrate our basic idea to take direct advantage of heat transfer, which dominates microscale systems, to enhance lift, reduce drag, and increase the envelope of operation of airfoils. For example, it is predicted that for an airfoil with chord of 2 cm, in a flow with Mach number ∼0.0725, $T = 300$ K, and $Re \sim 3 \times 10^4$, a reduction of 100 K in airfoil upper surface temperature (200 K) compared to the flow temperature, coupled with a 100 K increase in lower surface temperature (400 K) may result in delay of stall and up to 190% improvement in sectional L/D ratios at high angles of attack (from 5.4 to 15.5 at 12-deg sectional angle of attack).

These results may help to advance the technology closer to the DARPA goal of uninterrupted MAV flight of 60 min. Our computational and theoretical studies indicate that control of surface temperature has the potential to lead to very significant improvements in aerodynamic efficiency of microscale airfoils. The experimental investigations using a Peltier device that enforces a 70 K temperature differential between the upper and lower surfaces demonstrate the validity of the computational studies. For example, at an effective angle of attack of 4.5 deg, the estimated increase of lift coefficient is 6.0% with an upper surface temperature of 290 K and lower surface temperature of 360 K and −5.8% with an upper surface temperature of 360 K and lower surface temperature of 290 K. The experimental results show 7.7 and −7.7% for each case. The test data and numerical simulations show good correlation over a range of sectional angles of attack. The asymptotic model developed also provides good approximation to the numerical simulations. This model will provide further insight into the mechanism of heat transfer to improve aerodynamic performance of small-scale airfoils and will provide a convenient platform for performing parametric and design optimization studies.

References

[1]Grasmeyer, J. M., and Keenon, M. T., "Development of Black Widow Micro-Air-Vehicle," *Fixed and Flapping Wing Aerodynamics for Micro Air Vehicle Applications*, edited by Thomas J. Mueller, Vol. 195, Progress in Astronautics and Aeronautics, AIAA, Reston, VA, 2001, pp. 519–535.

[2]Samuel, P., Sirohi, J., Rudd, L., Pines, D., and Perel, R., "Design and Analysis of a Micro Coaxial Rotorcraft," *Proceedings of American Helicopter Society Vertical Lift Design Conference*, American Helicopter Society, Alexandria, VA, Jan. 2000.

[3]Page, D., "Micro-Air-Vehicles: Learning from Birds and Bees," *High Technology Careers Magazine*, Feature Presentation, URL: http://www.hightechcareers.com/doc198e/mav198e.html.

[4]Lipera, L., Colbourne, J., Tischler, M., Mansur, M., Rotkowitz, M., and Patangui, P., "The Micro Craft iSTAR Micro Air Vehicle: Control System Design and Testing," *Proceedings of AHS 57th Annual Forum*, American Helicopter Society, Alexandria, VA, 2001, pp. 1998–2008.

[5]Mueller, T. J., and Jansen, B. J., "Aerodynamic Measurements at Low Reynolds Numbers," AIAA Paper 82-0598, March 1982.

[6]O'Meara, M. M., and Mueller, T. J., "Laminar Separation Bubble Characteristics on an Airfoil at Low Reynolds Numbers," *AIAA Journal*, Vol. 25, No. 8, 1987, pp. 1033–1041.

[7]Mueller, T. J., and Burns, T. F., "Experimental Studies of the Eppler-61 Airfoil at Low Reynolds Numbers," AIAA Paper 82-0345, Jan. 1982.

[8]Kim, J., and Koratkar, N., "Aerodynamic Design Considerations for Micro-Rotorcraft," *Proceedings of the AHS 58th Annual Forum and Technology Display*, American Helicopter Society, Alexandria, VA, 2002, pp. 2181–2196.

[9]Young, L., Aiken, E., Johnson, J., Demblewski, R., Andrews, J., and Klem, J., "New Concepts and Perspectives on Micro-Rotorcraft and Small Autonomous Rotary-Wing Vehicles," *Proceedings of the 20th AIAA Applied Aerodynamics Conference*, AIAA, Reston, VA, 2002.

[10]Bohorquez, F., Samuel, P., Sirohi, J., Pines, D., Rudd, L., and Perel, R., "Design, Analysis and Hover Performance of a Rotary Wing Micro Air Vehicle," *Journal of the American Helicopter Society*, Vol. 48, No. 2, 2003, pp. 80–90.

[11]Zbikowski, R., "Flapping Wing Technology," European Rotorcraft Helicopters Symposium, March 2000.

[12]Zbikowski, R., Pedersen, C., Hameed, A., Friend, C., and Barton, P., "Current Research on Flapping Wing Micro Air Vehicles at Srivenham," *AVT Symposium on Unmanned Vehicles for Aerial, Ground and Naval Military Operations*, NASA Center for AeroSpace Information (CASI), Hanover, MD, 2000.

[13]Rusak, Z., "Subsonic Flow Around the Leading Edge of a Thin Aerofoil with a Parabolic Nose," *European Journal of Applied Mathematics*, Vol. 5, 1994, pp. 283–311.

[14]Maruyama, S., Nino, E., and Ruocco, G., "Analysis of a Thermo Electrical Device for Active Heat Transfer Control," *International Journal of Thermal Sciences*, Vol. 40, No. 10, 2001, pp. 911–916.

[15]Coulliette, C., and Plotkin, A., "Aerofoil Ground Effect Revisited," *Aeronautical Journal*, Vol. 100, No. 992, 1996, pp. 65–74.

[16]Leishman, J. G., *Principles of Helicopter Aerodynamics*, Cambridge Univ. Press, Cambridge, England, U.K., 2000, Chap. 3.

A. Plotkin
Associate Editor